New Journal of Physics
The open-access journal for physics

Simulation of vibrational resonances of stiff AFM cantilevers by finite element methods

F J Espinoza-Beltrán[1], K Geng[2], J Muñoz Saldaña[1], U Rabe[2], S Hirsekorn[2,3] and W Arnold[2,4]

[1] Centro de Investigación y Estudios Avanzados del Instituto Politécnico Nacional. Unidad Querétaro, Apdo. Postal 1-798, 76001 Querétaro, Qro., Mexico

[2] Fraunhofer Institute for Non-Destructive Testing (IZFP), Campus E 3.1, D-66123 Saarbrücken, Germany

E-mail: sigrun.hirsekorn@izfp.fraunhofer.de

New Journal of Physics **11** (2009) 083034 (22pp)
Received 1 April 2009
Published 28 August 2009
Online at http://www.njp.org/
doi:10.1088/1367-2630/11/8/083034

Abstract. We report on the simulation of vibrational resonances of stiff atomic force microscope cantilevers made of silicon by finite element methods (FEM) for application in contact-resonance spectroscopy. The FEM model considers the cubic symmetry of silicon single crystals and the geometrical shape of the cantilevers with a trapezoidal cross section and a triangular free end. Using a two-step iterative procedure, we fitted our FEM model to the experiment. In a first step, we used the measured resonant frequencies of an individual cantilever to fit the geometrical dimensions of the cantilever beam model. In a second step, we measured the resonant frequencies of the same cantilever in contact with a sample and determined the out-of-plane and in-plane tip–sample contact stiffness values by a fitting procedure. The FEM model also allows precise calculation of the spring constant of the cantilever, and consequently calculation of the force in contact. Finally, we compared the contact stiffness values with those predicted by contact mechanics models.

[3] Author to whom any correspondence should be addressed.

[4] Present address: Department of Materials, University of the Saarland, Campus D 2.2, D-66123 Saarbrücken, Germany.

Contents

1. Introduction

Atomic force microscopy (AFM) is a useful tool for materials characterization with a spatial resolution at the nanoscale level [1]. The AFM sensor is a flexible micro-beam with a sensor tip at its end. Commercially available cantilevers are made of silicon single crystals by micromachining technology following some preferential cleavage planes. AFM and its modifications have been intensely used for obtaining high-resolution images of topography and other surface properties such as e.g. adhesion, friction, electric and magnetic forces, ferroelectric polarization, and mechanical stiffness [2] probed by the cantilever tip in contact, intermittent contact, or non-contact with the sample by means of bending or torsion of the beam. High frequency ($\approx$100 kHz–3 MHz) dynamic techniques like atomic force acoustic microscopy (AFAM) ([3] and references cited therein) or ultrasonic atomic force microscopy (UAFM) [4, 5] which combine AFM with ultrasound are particularly suitable for stiffness and elastic or viscoelastic measurements. These techniques are based on contact-resonance spectroscopy, i.e. they exploit the resonance spectra of vibrating AFM cantilever beams when the tip is in contact with a sample surface.

Contact-resonance vibrations of the cantilever can be excited either by a vibration of the sample surface, which in turn is excited by an ultrasonic transducer coupled to the sample (AFAM) or by a vibration of the cantilever holder (UAFM) or the cantilever itself. Caused by the forces acting between the tip and the sample surface, the contact-resonance frequencies of the bending, torsional and lateral modes of the cantilever shift relative to its free vibration spectra. If an excitation frequency near a flexural contact-resonance is applied and, while scanning a sample surface, the amplitude and phase of the resulting cantilever vibration is recorded by lock-in-techniques, an elastic stiffness image of the surface is obtained. The spatial resolution depends on the tip–sample contact radius, which is usually in the range from 10 to 100 nm. For quantitative evaluation, complete contact-resonance spectra have to be measured [6]. The contact-resonance frequencies of the cantilever provide the tip–sample contact stiffness [3]–[6], which depends on the elastic indentation moduli of the tip and the sample and on the shape of contact.

The quantitative analysis procedure requires a convenient analytical or numerical model. Analytical models describing the free cantilever-vibration as well as the contact-resonances assuming AFM cantilever beams of constant cross section and rigid clamping at one side are well known ([7] and references cited therein). This approach works well to describe the overall behavior of the vibration modes. However, the resonances of most of the cantilevers show slight systematic deviations from the analytical models, and the theoretical frequencies cannot be fitted to two or more experimental free bending modes simultaneously with an error in the resonance frequencies of less than 10%. This holds especially for stiff cantilevers with spring constants of about 5–50 Nm^{-1}, which are used for contact-resonance applications [8]. Furthermore, the analytic description of the cantilever vibrations used so far in the literature reproduces the contact-resonance frequencies with accuracies of less than 20% [3], [6]–[9]. Therefore, a more precise modeling shall improve the understanding of the oscillatory behavior of the cantilever in AFAM measurements and help to quantify the tip–sample interactions. Numerical modeling using the finite element method (FEM) seems to be an effective tool for this purpose, since it allows a more detailed description of the cantilever.

One-dimensional (1D) finite element and 3D beam element models have been used to simulate the AFM cantilever [10, 11], but they neglect important details of the geometric shape. Other simulations by ANSYS taking into account a more realistic geometrical shape of the cantilevers compared calculated vibration modes with experimental results in order to obtain precise static spring-constant values [12, 13]. A finite element model of triangular cantilevers was applied to measure shear stiffness [14], and tip effects on contact-resonance vibrations and modal sensitivities of triangular cantilevers were examined by FEM methods [15]. The dynamics of AFAM measurements were modeled by FEM in order to determine quantitatively elastic properties of thin films [16]. But this work does not consider the elasticity of the suspension of AFM cantilevers, which influences significantly the resonance frequencies [8]. A previous publication [17] presents the first FEM model of AFM cantilevers considering the actual features of its geometry, however, neglecting the elastic anisotropy of single-crystal silicon.

This paper presents a two-step FEM fitting procedure in order to simulate the vibrational resonances of single-crystal silicon cantilevers considering their most important geometrical details as well as their elastic anisotropy. The lowest bending, torsional and lateral bending modes of a free cantilever are measured as well as the first three bending modes with sample surface contact. The geometrical parameters of the FEM cantilever model are first fitted to reproduce the measured first and third free bending mode. Subsequently, tip length and cantilever declination were adapted to the measured contact-resonance frequencies of these two modes. With the obtained FEM cantilever model, the bending as well as the torsional resonances were predicted and compared with the experimental spectra. The objective of this work was to obtain an improved model for AFM cantilever vibration simulations allowing the prediction of resonance frequency shifts as a function of the tip–sample contact stiffness. This FEM approach should allow a higher precision in the determination of contact stiffness than previously achieved by using analytical models.

2. Description of the cantilever model

For the experiments described here, we used commercial atomic force microscope cantilevers made of silicon single crystals (Nanosensors, NanoWorld Services, Switzerland, ‘non contact long (NCL)’ beams). The dimensions of these cantilevers range from 146 to 236 μm $\times$ 30

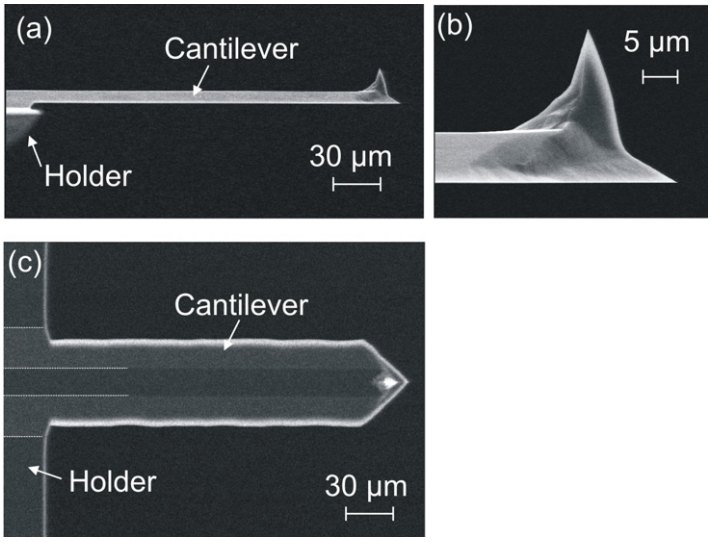

Figure 1. SEM micrographs showing (a) a side view of a cantilever, (b) an enlarged side view of the end of the cantilever carrying the sensor tip and (c) a view from the bottom side where the tip is mounted.

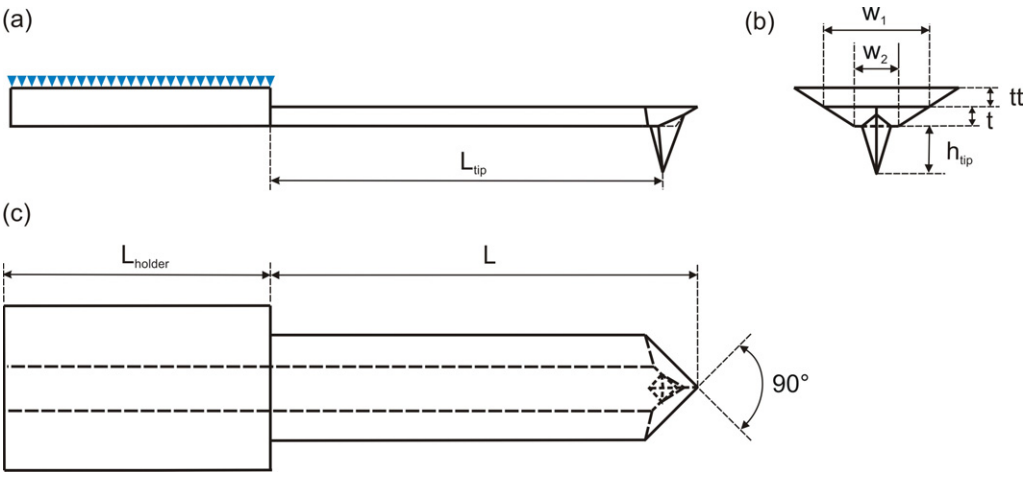

Figure 2. Schematic of the probe geometry used for the FEM simulations.

to 45 μm × 6 to 8 μm (length × width × thickness) with spring constants from 21 to 98 N m^{-1}. Scanning electron microscope (SEM) micrographs of such a cantilever are shown in figure 1 [18]. The trapezoidal cross section and the triangular end of this type of beam, which result from batch fabrication by anisotropic etching, are clearly visible. The protruding free part of the cantilever continues on top of the holder as a strip with trapezoidal cross section. A small part of the holder, to which the cantilever is fixed, is visible at the left side of figures 1(a) and (c).

Our FEM model contains the main geometrical features of the NCL sensors. A schematic representation of this model is shown in figure 2. The probe is described as a beam with trapezoidal cross section and a triangular free end. The cantilever has a total length L. The sensor tip position is L_{tip} and the tip length is h_{tip}. The cross section of the beam has an upper

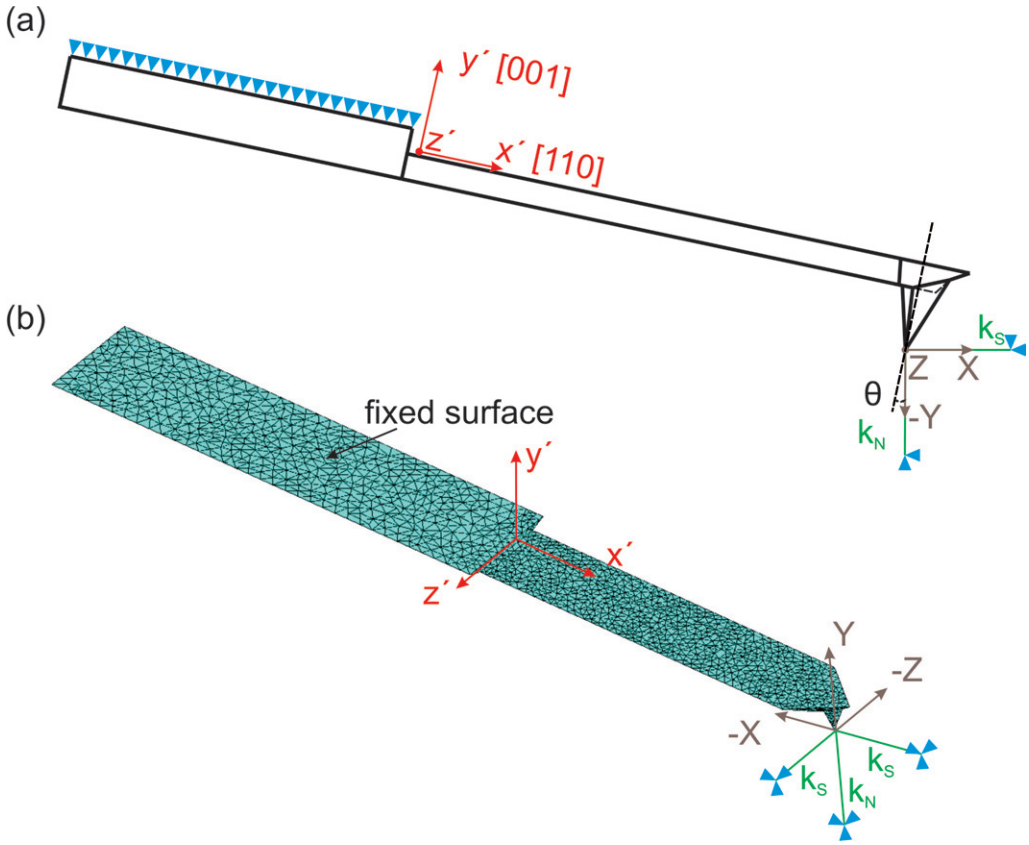

Figure 3. Schematic of the cantilever (a) with its coordinate system $\{x',y',z'\}$ inclined by an angle θ relative to the sample surface coordinate system $\{X, Y, Z\}$. The tip–sample forces are modeled by three springs with spring constants k_N and k_S for vertical and lateral contact stiffness, respectively; (b) FEM model of the cantilever after meshing.

width w_1, a bottom width w_2 and a thickness t. In order to model the clamping conditions of the cantilever suspended at the holder, we extended the cantilever by an element with trapezoidal cross section, length L_{holder} and thickness $tt + t$. The top surface of this extension is rigidly fixed (figure 2(a)).

For the description of the cantilever, we used a Cartesian coordinate system with the x'-, y'- and z'-axes in the cantilever length, thickness and width directions, respectively (figure 3). These axes coincide with the crystallographic axes [110], [001] and $[1\bar{1}0]$ of the cubic single crystal material, respectively. The length axis of the cantilever is not parallel to a cube edge of the silicon single crystal, but to a face diagonal. We rotated the matrix of elastic constants accordingly for our FEM model as shown in appendix A. The rotated matrix contains six different elastic constants instead of 3, consequently the symmetry of the material in the cantilever coordinate system is tetragonal. The elastic constants for the rotated coordinate system are $E'_x = E'_z = 169.7\,\text{GPa}$, $E'_y = 130.4\,\text{GPa}$, $\nu'_{xy} = \nu'_{zy} = 0.362$, $\nu'_{yz} = \nu'_{yx} = 0.278$, $\nu'_{xz} = \nu'_{zx} = 0.061$, $G'_{xy} = G'_{yz} = 80.0\,\text{GPa}$ and $G'_{zx} = 51\,\text{GPa}$ (see appendix A, the single crystal elastic constants given there correspond to Young's moduli of the cantilevers given by the manufacturer). These values and the mass density of silicon $\rho_{\text{Si}} = 2330\,\text{kg}\,\text{m}^{-3}$ were used in the FEM simulations.

Table 1. Experimentally measured geometrical parameters of the cantilever compared with those obtained by fitting the FEM model to the free vibrations. The parameters $h_{\text{tip}} = 13\,\mu$m, $L_{\text{holder}} = 300\,\mu$m, $tt = 4.0\,\mu$m and $\theta = 12^\circ$ were fixed.

Parameter	Measured values	FEM values	Relative difference (%)
$L\,(\mu\text{m})$	234.9 ± 3.0	235.2	0.13
$w_1\,(\mu\text{m})$	54.2 ± 0.8	54.2	0.08
$w_2\,(\mu\text{m})$	18.9 ± 0.9	18.8	0.71
$t\,(\mu\text{m})$	6.7 ± 0.1	6.6	1.57

The simulations were carried out with the commercial finite element modeling (FEM) software (ANSYS-Engineering Analysis System V10) [19]. The bulk of the cantilever and the tip were approximated by SOLID95 3D elements. The FEM model comprises 6221 elements with linear dimensions of about 1.5 μm on average for both the beam and the tip. In the regions where higher strain was to be expected, the density of the grid elements was increased, as shown in figure 3(b). The modal analysis problem was solved by means of the 'Block–Lanczos method', which was derived to solve classical eigenvalue problems and is described in detail in the literature [20].

For practical reasons, the length axis of AFM cantilevers inclines by an angle θ toward the sample surface. We modeled the tip–sample contact forces as three springs in a coordinate system $\{X, Y, Z\}$ aligned to the sample surface (figures 3(a) and (b)). The coordinate system $\{X, Y, Z\}$ was chosen to coincide with the cantilever system $\{x', y', z'\}$ for $\theta = 0^\circ$. The spring constants k_{N} and k_{S} are the tip–sample contact stiffness values in out-of-plane (Y-axis) and in-plane direction (X- and Z-axes). In our FEM model, we used three 1D elements COMBIN14 to represent the tip–sample contact in the three orthogonal directions relative to the sample surface, each with its characteristic spring constant as well as its damping coefficient. In the numerical simulation, a stiff tip (elastic constants $\approx 10^5$ GPa) was assumed in order to avoid an unrealistically large deformation of the tip end due to the contact forces acting like a point load.

3. Fitting of the FEM model to an individual cantilever

One individual non-contact long (NCL) AFM cantilever (NCL 52461F2L406, probe no. 2) was characterized by optical and scanning electron microscopy by the manufacturer to obtain its geometrical data [18]. Additionally, we measured its geometrical dimensions in an optical microscope. The averaged geometrical data are listed in table 1. A precision of 0.1–3 μm of the geometrical data was achieved. This measurement error led to an error of at least several kHz in frequency using analytical models for resonance frequency calculations (table 2). We assume a similar error from geometrical uncertainty if FEM analysis is used. However, the resonance frequencies of a cantilever can be measured with a precision better than 1%, because the quality factor of the experimental resonance curves in air is close to 200 or higher (see table 2). The free resonances of the cantilever were measured by exciting the cantilever holder with an ultrasonic transducer, sweeping the excitation frequency and measuring the forced cantilever vibration by an interferometer [21]. We obtained resonance spectra including bending, torsional and lateral vibration modes of the cantilever (table 2).

Table 2. Experimental resonance frequencies of the cantilever and the corresponding quality factors, values obtained with FEM simulation, and values obtained with analytical models; (B) denotes bending, (L) lateral and (T) torsional modes. For the calculations, the parameters of table 1 were used. The errors in the analytically calculated frequencies follow from the measuring inaccuracies in the geometrical data in table 1.

Vibrational modes	Experimental frequencies (kHz)	Experimental quality factor Q	Frequencies from FEM model (kHz)	Relative difference to exp. (%)	Frequencies from analytical models (kHz)	Relative difference to exp. (%)
B1	169.84	539	169.72	0.07	167.44 ± 7.57	1.41
L1	974.993	969	1021.5	4.77	1056.0 ± 46.9	8.31
B2	1048.42	639	1050.1	0.16	1049.3 ± 47.4	0.08
T1	1531	824	1541.9	0.71	1457.7 ± 62.4	4.79
B3	2876.73	228	2888.6	0.41	2938.2 ± 132.8	2.14
T2	4519.8	188	4579.9	1.33	4373.1 ± 184.9	3.25

We used an optimization procedure in ANSYS, the sub-problem method [22], to fit the geometrical parameters of the FEM cantilever model for optimized agreement with the experimental resonances. This optimization procedure is an advanced zero-order method with the dependent and the fixed variables as well as the measured resonance frequencies as input. For the dependent variables, first least-square fits were chosen and the constrained minimization problem was converted to an unconstrained problem using penalty functions. Then, the approximated and penalized function are minimized in each iteration step (equivalent to one complete analysis loop) until convergence is achieved or termination is indicated.

To adapt the free cantilever vibration behavior, we varied the parameters length L, width w_1, w_2, and thickness t in the FEM model within a range close to the experimental values. The aim was to obtain the best fit to the measured resonance frequencies of the first (B1) and third (B3) free bending mode. The second bending mode (B2) was not considered, because there is an overlap of the spectra of the first lateral (L1) and the second bending (B2) mode, so that they cannot easily be distinguished in numerical calculations. The parameters $h_{\mathrm{tip}} = 13\,\mu$m, $L_{\mathrm{holder}} = 300\,\mu$m, $tt = 4.0\,\mu$m, and $\theta = 12^\circ$ were kept constant during the first fitting procedure. The error of the fitting is defined by the error function

$$\mathrm{Error}(f_1, f_3)[\%] = 50\left(\frac{|f_1 - f_{\mathrm{B1}}|}{f_{\mathrm{B1}}} + \frac{|f_3 - f_{\mathrm{B3}}|}{f_{\mathrm{B3}}}\right). \tag{1}$$

Here, the frequencies f_1 and f_3 are calculated by the FEM model, and f_{B1} and f_{B3} are the measured resonance frequencies of the modes B1 and B3, respectively. The minimum value of $\mathrm{Error}(f_1, f_3)$ corresponds to a set of model parameters. The fitting procedure was stopped when a minimum value of the error function lower than 1.0% was found.

Besides the average values of the measured geometrical parameters of the cantilever, table 1 shows the results of the FEM fitting procedure. In table 2, the measured resonance frequencies of six vibration modes are compared with the corresponding values following from the fitted FEM model as well as from analytical models, and the quality factor Q of the resonances determined

from the width of the measured resonance curves is given. The measurements have been carried out under laboratory conditions in air.

Analytical models to calculate beam vibrations are well known [7, 8, 13, 23]. Using a fourth-order partial differential equation of motion, the flexural resonance frequencies f_{nf} are derived for homogeneous clamped-free beams with constant symmetric trapezoidal cross section

$$f_{\mathrm{nf}} = \frac{(\alpha_{\mathrm{nf}} L_{\mathrm{eff}})^2}{2\pi L_{\mathrm{eff}}^2} \sqrt{\frac{EI}{\rho A}}, \tag{2}$$

where E is the Young's modulus in the [110]-direction of single crystal silicon ($E = E'_x$), ρ is the density of silicon, $I = t^3((w_1+w_2)^2 + 2w_1w_2)/(36(w_1+w_2))$ is the area moment of inertia of a beam with symmetric trapezoidal cross section and $A = t(w_1+w_2)/2$ is the cross-sectional area. If damping is neglected, the normalized wave numbers are $\alpha_{\mathrm{nf}} L_{\mathrm{eff}} = \{1.8751, 4.6941, 7.8548, 10.9954, \ldots\}$. Here, an effective length of the cantilever $L_{\mathrm{eff}} = L - t/\sqrt{2}$ is used, because this analytical model only holds for constant cross sections. The torsional resonance frequencies f_{tnf} are derived from a second-order partial differential equation

$$f_{\mathrm{tnf}} = \frac{2n-1}{4L_{\mathrm{eff}}} \sqrt{\frac{C_{\mathrm{t}}}{\rho I_{\mathrm{P}}}}, \tag{3}$$

where $I_{\mathrm{P}} = t^3((w_1+w_2)^2 + 2w_1w_2)/(36(w_1+w_2)) + t(w_1+w_2)(w_1^2+w_2^2)/48$ is the polar area moment of inertia and C_{t} is the torsional stiffness of a beam with symmetric trapezoidal cross section (appendix B). The analytical results in table 2 follow from equations (2) and (3). For the calculation of the lateral bending mode L1, equation (2) is used with interchanged cantilever width and thickness. This entails the large deviation of the analytically calculated lateral bending resonance in comparison to the experimental value, because in this case, the presumption that the width has to be large compared with the thickness used in the derivation of equation (2) is not fulfilled.

The comparison of the results in table 2 clearly shows a better agreement between theoretical and experimental frequencies for the FEM than for the analytical calculations, though we used refined analytical models considering of the trapezoidal cross section.

To fit the experimental resonance frequencies of the free cantilever vibrations (three bending modes and two torsional modes, given in table 2) only the four parameters L, w_1, w_2, t (table 1) were used. In this step, the parameters $h_{\mathrm{tip}} = 13\,\mu$m, $L_{\mathrm{holder}} = 300\,\mu$m, $tt = 4.0\,\mu$m and $\theta = 12^\circ$ were fixed close to the expected values. Variations of these parameters do not significantly affect the free cantilever vibrations.

4. Fitting of the FEM model to measured contact-resonance frequencies

The second step of the fitting procedure is based on the comparison of the simulated resonance frequencies of the bending modes B1 and B3 to the corresponding experimental values of the contact-resonances. AFAM measurements were carried out on two samples of fused silica and single crystal nickel, respectively, increasing the static cantilever deflection from 0 to 60 nm and decreasing it again to zero, i.e. each measurement consisted of a loading and an unloading branch. The contact-resonance frequencies obtained from the spectra are plotted in figure 4 as full symbols (loading) and open symbols (unloading). We evaluated three measurements

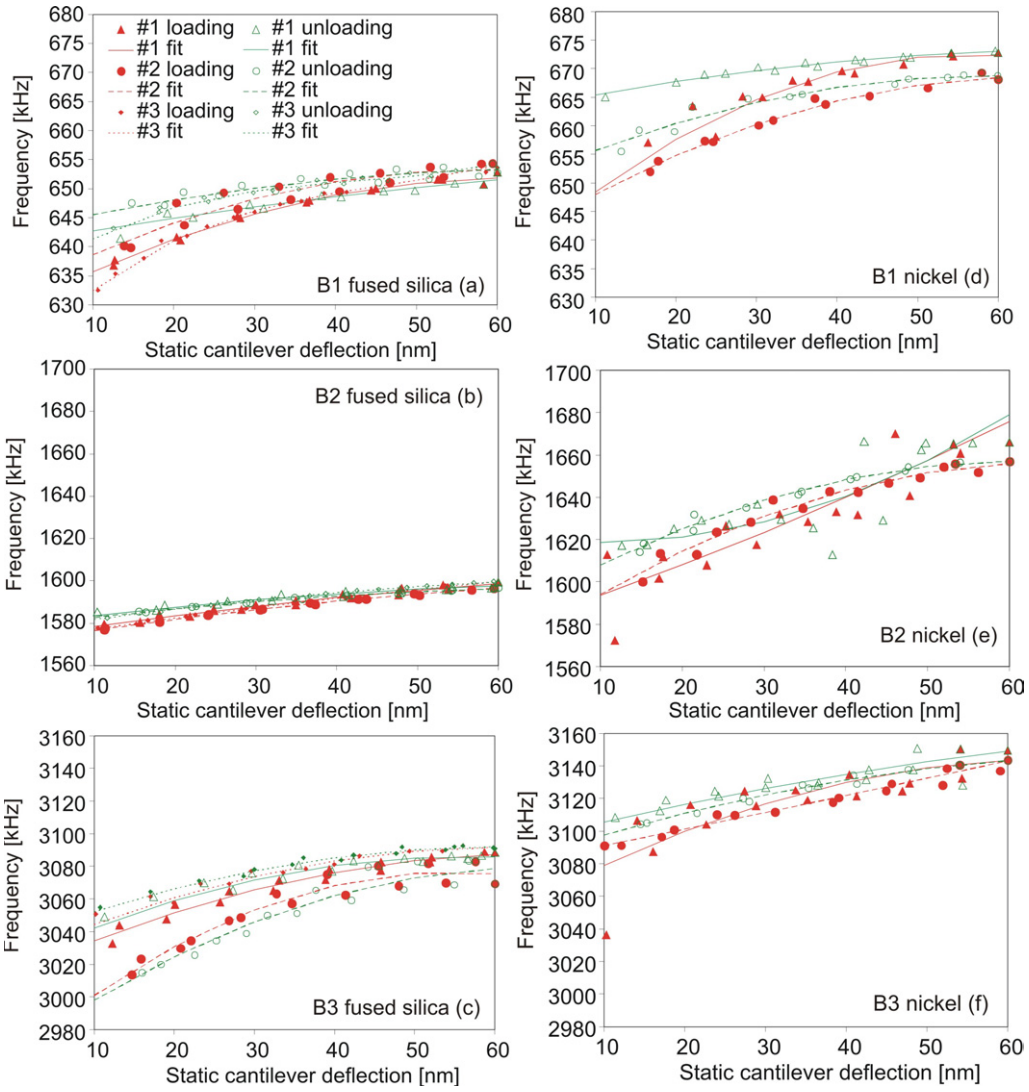

Figure 4. Contact-resonance frequencies obtained for the first, second and third bending modes (B1, B2 and B3) on a fused silica and on a nickel single-crystal sample. The full symbols designate the frequencies obtained during loading and the open symbols those obtained during unloading. The lines are fits with polynomial functions.

on fused silica (FS/1, FS/2 and FS/3) and two measurements on nickel (Ni/1 and Ni/2), respectively. The sequence of measurements was FS/1, Ni/1, FS/2, Ni/2 and FS/3. To simplify the analysis, we determined the resonance frequencies for static deflections of 30, 40, 50 and 60 nm by interpolating the experimental frequencies with polynomial functions (lines in figure 4). These values are listed in table 3. The data for static deflections less than 20 nm were not considered, because especially on fused silica a hysteresis is observed, as can be seen by comparing the frequencies for loading and unloading in figure 4.

The simulations were carried out with the geometrical parameters of the cantilever following from the FEM analysis of the free cantilever vibrations described in the previous section. The variables to be fitted were the angle of inclination θ (variation range 10–14°),

Table 3. Contact-resonance frequencies for the first three bending modes on fused silica and nickel for static cantilever deflections from 30 to 60 nm for increasing and decreasing load, respectively. The listed results are values interpolated from experimental data sets.

Sample/ measurement	Static cantilever deflection (nm)	Resonance frequencies for increasing static load			Resonance frequencies for decreasing static load		
		f_{B1} (kHz)	f_{B2} (kHz)	f_{B3} (kHz)	f_{B1} (kHz)	f_{B2} (kHz)	f_{B3} (kHz)
FS/1	60	651.84	1598.5	3087.3	651.52	1597.7	3085.8
	50	650.94	1595.5	3083.3	650.18	1596.0	3085.2
	40	648.88	1592.2	3076.0	648.64	1593.7	3080.5
	30	645.64	1588.0	3065.4	646.88	1590.9	3071.7
Ni/1	60	672.32	1675.7	3143.5	673.03	1678.9	3149.1
	50	671.95	1657.3	3138.7	672.29	1657.2	3142.5
	40	669.37	1639.8	3129.8	671.16	1640.3	3134.9
	30	664.58	1623.4	3116.9	669.64	1628.3	3126.2
FS/2	60	653.22	1596.6	3075.6	653.33	1596.3	3078.6
	50	652.84	1593.8	3075.7	652.71	1594.9	3073.0
	40	651.2	1590.4	3068.2	651.62	1592.8	3062.1
	30	648.28	1586.4	3053.3	650.06	1590.1	3045.9
Ni/2	60	668.41	1655.8	3143.1	668.75	1657.0	3143.2
	50	667.05	1651.6	3132.4	668.26	1654.5	3138.4
	40	664.33	1643.3	3121.8	666.71	1648.4	3131.4
	30	660.24	1631.0	3111.4	664.08	1638.5	3122.2
FS/3	60	653.97	1599.6	3091.7	654.21	1599.4	3091.9
	50	651.43	1595.9	3089.2	652.21	1597.3	3090.1
	40	649.27	1591.8	3083.2	651.05	1594.4	3085.2
	30	646.23	1587.3	3073.2	649.60	1590.9	3077.3

tip length h_{tip} (variation range 10–15 μm) and contact stiffness values k_N (variation range 100–3000 N m^{-1}) and k_S (variation range 0–2000 N m^{-1}). Tip length and angle of inclination are varied within their typical ranges of commercial NCL cantilever beams as extracted from high resolution SEM pictures (as e.g. figure 1). An essential objective of FEM modeling of AFM cantilevers was to yield a procedure avoiding the need of high resolution SEM pictures of each single AFM cantilever used for AFAM measurements. We assumed that the stiffness values were the same for both bending modes B1 and B3 if the measurements were carried out on the same material and at the same cantilever static deflection. The fitting procedure was stopped and considered to be successful when the calculated resonance frequencies deviated less than 1.0% from the experimental values. Equation (1) was used to define the deviation between experimental and calculated frequencies. Table 4 lists the results of the best fits for the parameters h_{tip}, θ, k_S, and k_N. The calculated resonance frequencies for the bending modes B1, B2 and B3 and the corresponding error functions are listed in table 5.

As the values of the contact stiffnesses k_S and k_N were obtained from the best fit of the FEM model to the experimental resonance frequencies, the error function is also a measure of the error

Table 4. Parameters tip length h_{tip}, inclination angle θ, in-plane contact stiffness k_S and normal contact stiffness k_N obtained as a result of the fitting procedure.

		Fitted parameters for increasing static load				Fitted parameters for decreasing static load			
	Stat. defl. (nm)	h_{tip} (μm)	θ (deg)	k_S (N m^{-1})	k_N (N m^{-1})	h_{tip} (μm)	θ (deg)	k_S (N m^{-1})	k_N (N m^{-1})
FS/1	60	11.948	11.549	7.7871	1434.4	11.672	12.223	8.2974	1428.9
	50	12.286	12.287	3.2677	1402.6	11.350	13.584	153.620	1409.1
	40	12.388	12.624	20.546	1359.9	12.503	13.414	88.759	1353.6
	30	13.710	11.120	5.2527	1344.7	11.103	13.819	5.5703	1354.3
Ni/1	60	12.904	11.532	72.749	1813.3	12.825	11.785	127.07	1819.5
	50	12.865	13.038	61.339	1801.6	12.822	13.085	28.704	1835.9
	40	12.733	12.278	60.755	1754.8	12.680	12.156	94.950	1800.9
	30	12.550	12.263	12.319	1666.0	12.721	12.277	49.112	1756.3
FS/2	60	14.481	11.229	54.984	1420.8	13.383	12.894	26.220	1420.4
	50	12.855	13.118	5.7078	1418.9	14.143	11.024	8.6295	1413.6
	40	13.269	13.091	5.7363	1391.5	13.546	12.857	5.7249	1393.8
	30	12.814	13.193	4.5500	1347.3	14.374	11.020	5.9205	1382.8
Ni/2	60	12.921	11.934	116.23	1744.2	12.536	12.184	167.11	1744.9
	50	12.918	12.145	30.816	1704.9	12.821	12.158	38.850	1757.9
	40	12.799	12.142	38.482	1640.2	12.606	11.635	114.92	1690.4
	30	12.309	12.132	15.277	1589.1	12.811	11.736	152.64	1633.5
FS/3	60	11.231	11.362	46.225	1457.9	11.088	12.002	124.78	1473.3
	50	11.452	11.548	72.635	1430.1	12.726	12.273	108.40	1421.4
	40	11.832	11.222	3.6047	1390.6	11.543	12.100	9.2717	1420.4
	30	11.842	12.329	0	1346.3	12.825	11.590	10.642	1387.7

bars of the stiffnesses, i.e. they are lower than 1.0% and comparable to or smaller than the size of the symbols in figure 6. To estimate the error of the calculated parameters based on experimental error sources, additional calculations varying the experimental resonance frequencies within the width of the resonance peak have to be carried out. This is not considered in this work.

The average values of h_{tip} and θ and the scattering of the results including all measurements on fused silica and on nickel are $12.5 \pm 1.1\,\mu$m and $12.3 \pm 0.8^\circ$, respectively. Despite the scattering of about 10% around the average values, the corresponding error values obtained from the FEM calculations are always lower than 1.0%. In order to examine the influence of h_{tip} and θ, in figure 5(a) group of curves of constant error function varying h_{tip} and θ in the range from 8.0 to 16.5 μm and from 10.0 to 17.0°, respectively, is shown. The calculations were carried out with the experimental data of the first measurement on fused silica for increasing static load for a static deflection of 60 nm, for which the contact stiffness values k_S and k_N of 7.78 and 1434.4 N m^{-1}, respectively, were obtained. The results in figure 5 indicate that the parameters h_{tip} and θ do not play a relevant role for the modeling of the cantilever vibration in sample contact, when the geometrical parameters L, w_1, w_2 and t were previously determined by the free cantilever vibrations. Increasing the inclination angle as well as the tip length causes an increase of the lateral part in the tip–sample interaction forces during flexural cantilever

Table 5. Resonance frequencies $f_{Bi}(i = 1, 2, 3)$ of the first three bending modes B1, B2 and B3 obtained by fitting the FEM model for the individual measurements and the corresponding values of the error function.

		Fitted frequencies for increasing static load				Fitted frequencies for decreasing static load			
	Stat. defl. (nm)	f_{B1} (kHz)	f_{B2} (kHz)	f_{B3} (kHz)	Error (%)	f_{B1} (kHz)	f_{B2} (kHz)	f_{B3} (kHz)	Error (%)
FS/1	60	651.61	1543.9	3097.7	0.19	651.64	1544.2	3095.8	0.17
	50	650.51	1543.9	3088.7	0.12	650.82	1544.2	3098.2	0.26
	40	648.08	1543.8	3078.6	0.10	648.62	1542.4	3080.6	0.01
	30	647.00	1542.9	3074.9	0.28	647.01	1540.1	3078.1	0.11
Ni/1	60	670.31	1543.4	3158.5	0.40	670.93	1543.5	3162.3	0.37
	50	671.06	1543.5	3145.7	0.17	672.18	1543.5	3148.2	0.11
	40	668.61	1543.8	3145.0	0.30	670.43	1543.7	3156.2	0.39
	30	664.52	1543.8	3128.5	0.19	668.61	1543.8	3144.4	0.37
FS/2	60	652.79	1542.7	3086.5	0.20	653.02	1543.5	3081.7	0.07
	50	652.54	1543.7	3081.6	0.11	651.77	1542.9	3084.3	0.26
	40	650.99	1543.3	3073.9	0.11	651.47	1543.4	3075.0	0.22
	30	647.9	1536.0	3069.8	0.30	650.06	1542.7	3077.9	0.52
Ni/2	60	668.37	1543.6	3148.8	0.10	668.31	1543.7	3153.2	0.19
	50	666.42	1543.6	3133.9	0.08	668.63	1543.7	3144.0	0.12
	40	663.45	1543.5	3124.8	0.11	665.32	1543.6	3142.7	0.29
	30	660.56	1543.8	3118.2	0.14	663.31	1543.5	3134.7	0.27
FS/3	60	652.58	1544.3	3110.7	0.41	653.57	1544.2	3115.1	0.42
	50	651.08	1544.0	3104.5	0.28	652.24	1543.5	3095.7	0.09
	40	648.72	1543.9	3092.5	0.19	650.84	1544	3095.3	0.18
	30	646.74	1543.5	3080.5	0.14	649.47	1543.3	3084.4	0.13

vibrations, so that in tip–sample contact modeling the effect of an increasing inclination angle can be compensated by decreasing the tip length and vice versa. That is, in future measurements h_{tip} and θ can be assumed as fixed when using the same cantilever, and one single measurement on a reference sample is sufficient to determine them without introducing a significant error in the quantitative analysis.

5. Spring constant of the cantilever

After matching the experimental and the simulated resonance behavior of the cantilever by the fitting procedure, the FEM model allows the calculation of the static spring constants of the sensor. We simulated stepwise increasing static loads acting in different directions on the cantilever at the tip position L_{tip}. The spring constants were derived from the slopes of the simulated load-displacement curves using the FEM values of the geometrical dimensions of the cantilever listed in table 1, which were obtained from modeling the free cantilever vibrations. The errors that may result from inaccuracies of the experimental free cantilever resonance frequencies are not considered so far.

If the cantilever is not inclined (i.e. $\theta = 0°$), the static loads ΔF_X, ΔF_Y and ΔF_Z are applied parallel to the axes x', y', and z', respectively, of the coordinate system of the

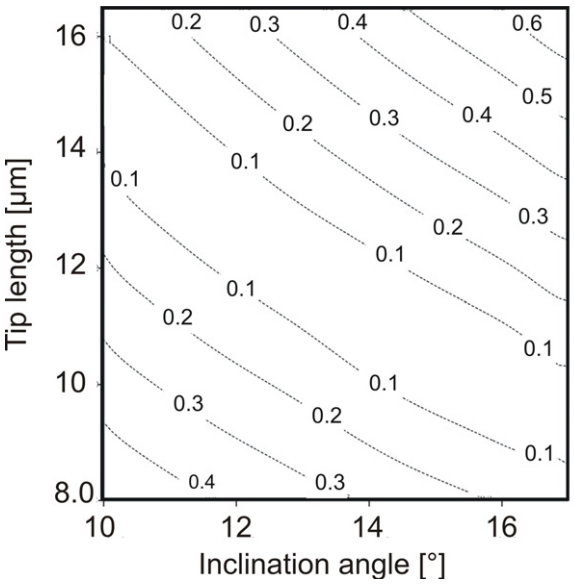

Figure 5. Plot of level curves of the error function as a function of h_{tip} and θ, varying from 8.0 to 16.5 μm and from 10.0 to 17.0°, respectively.

cantilever. The corresponding spring constants k_{i} obtained from the ratios $\Delta F_i/\Delta U_i$ (ΔU_i is the displacement of the cantilever along the i-axis) are $k_{x'} = 2162.5\,\text{N m}^{-1}$, $k_{y'} = 33.5\,\text{N m}^{-1}$, and $k_{z'} = 866.5\,\text{N m}^{-1}$, respectively. Based on a beam model with averaged dimensions and an isotropic elastic modulus, the manufacturer provides an estimated value $k_{y'} = 42\,\text{N m}^{-1}$ for the normal spring constant of this particular cantilever. The FEM result is about 20% lower.

Considering the previously obtained cantilever inclination of $\theta = 12.3°$ relative to the X-axis, the spring constants must be recalculated if forces normal or parallel to the sample surface are applied. In the coordinate system of the sample $\{XYZ\}$, we obtained the spring constants $k_X = 320.3\,\text{N m}^{-1}$, $k_Y = 36.8\,\text{N m}^{-1}$, and $k_Z = 866.5\,\text{N m}^{-1}$. The vertical stiffness k_Y increases by 9.85% relative to the case with zero inclination angle. A remarkable decrease of the stiffness in longitudinal direction (X-axis) of about 85.2% is observed as well, whereas the stiffness $k_{z'} = k_Z$ remains because the z'- and Z-axis coincide.

6. Analysis of the tip–sample contact

Figure 7 shows the variation of the out-of-plane contact stiffness k_{N} as a function of the static cantilever force for the tip in contact with fused silica and nickel, as obtained by FEM fitting (table 4). The static force F_{N} was calculated using the normal force constant $k_Y = 36.8\,\text{N m}^{-1}$ multiplied with the static deflection of the cantilever. For both samples, the contact stiffness increases with static load. The scattering of the fused silica data is lower than that of the nickel data (1.4 and 3.5%, respectively), which can be attributed to the homogeneous and isotropic properties as well as to the lower roughness of the fused silica sample.

In figure 7, the normal contact stiffness calculated with the Hertzian contact model [24] is also plotted for comparison. A spherical sensor tip with a radius R of 80 nm was assumed. The chosen value is of typical size and yields results close to the measured resonances, i.e.

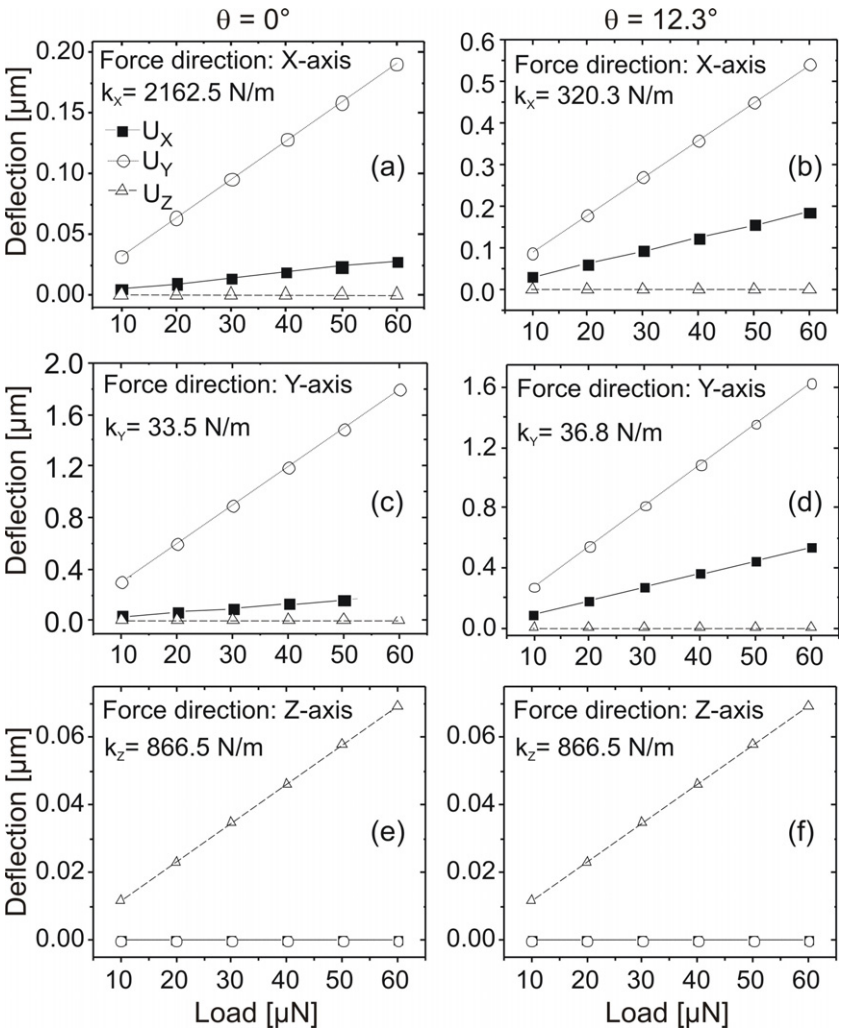

Figure 6. Static deflections U_X, U_Y, and U_Z of the cantilever in X-, Y- and Z-direction, respectively, as function of applied load in directions along (a) and (b) the X-axis, (c) and (d) the Y-axis and (e) and (f) the Z-axis. The plots (a), (c) and (e) correspond to a cantilever–oriented parallel to the sample surface ($\theta = 0$), and (b), (d) and (f) belong to a cantilever inclined by an angle $\theta = 12.3°$.

shows the relation to the Hertzian model. As discussed in section 7, the subjects tip shape and wear still need detailed investigation. According to the Derjaguin, Muller and Toropov (DMT) model [24], the normal contact stiffness is given by

$$k_{\mathrm{N}} = \sqrt[3]{6RE^{*2}(F_{\mathrm{N}} + F_{\mathrm{adh}})}, \tag{4}$$

where E^* is the effective Young's modulus of the contact and F_{adh} is the adhesion force. In our AFAM experiments, care was taken to work with low adhesion forces ($F_{\mathrm{adh}} <$ 338 nN). In this context, low adhesion forces means forces small in comparison to the static load on the cantilever, which is controlled by its static deflection adjusted before dynamic measurements [9]. Therefore, the term F_{adh} was neglected, and equation (4) reduces to the Hertz

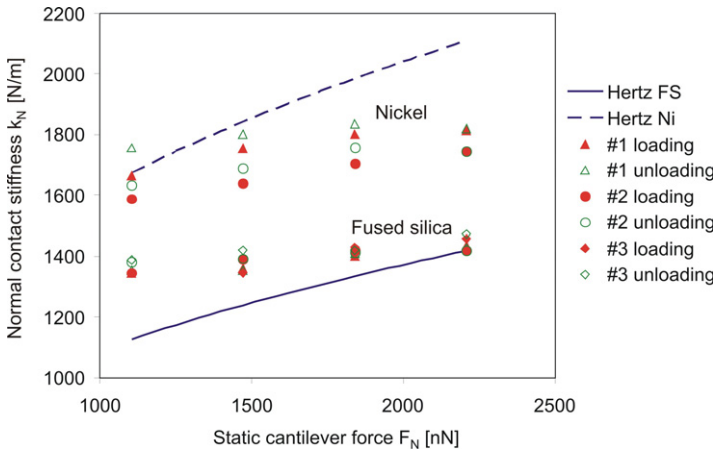

Figure 7. Out-of-plane contact stiffness k_N as a function of the static cantilever force obtained by FEM modeling of the AFAM measurements on fused silica and nickel presented in figure 4 and table 3. For comparison, the theoretical contact stiffness on nickel (dashed line) and on fused silica (full line) calculated with the Hertzian contact model is shown. A spherical sensor tip with a radius R of 80 nm was assumed.

formula. The reduced Young's modulus is $1/E^* = (1-\nu_{Tip}^2)/E_{Tip} + (1-\nu_{Surf}^2)/E_{Surf}$ in the case of elastic isotropic materials, where ν_{Tip}, ν_{Surf}, E_{Tip} and E_{Surf} are the Poisson's ratios and Young's moduli of the tip and the surface, respectively. In the case of elastic anisotropic materials and special symmetries, the reduced Young's modulus is given by $1/E^* = 1/M_{Tip} + 1/M_{Surf}$, where M_{Tip} and M_{Surf} are the indentation moduli [9, 25, 26] of the tip and the surface, respectively. The indentation moduli can be calculated from the elastic single-crystal constants of the materials [9, 25, 26]. In the case examined here, only the fused silica sample is isotropic ($\nu_{FS} = 0.17$, $E_{FS} = 73.6$ GPa;[5] $M_{FS} = E_{FS}/(1-\nu_{FS}^2) = 75.8$ GPa). The indentation moduli of the silicon tip $M_{Tip} = 165$ GPa (single crystal, 100-oriented) [9] as well as of the 100-oriented nickel single crystal, $M_{Ni} = 219$ GPa, were calculated using single crystal constants from the literature (silicon: $c_{11} = 166$ GPa, $c_{12} = 64$ GPa, $c_{44} = 80$ GPa; nickel: $c_{11} = 250$ GPa, $c_{12} = 160$ GPa, $c_{44} = 118.5$ GPa) [27, 28]. With these data and a tip radius R of 80 nm one obtains the two curves in figure 7, which represent the upper and the lower limit of the experimental data. This shows that the experimental contact stiffness values are in a reasonable range. However, the difference in contact stiffness between the two samples is smaller than predicted by contact mechanics, and the increase with static load is slower. The pressure in the tip–sample contact area is high enough in AFAM to cause a fracture of the tip, especially in contact with the nickel surface [29, 30]. A non-spherical tip shape, tip wear and the presence of oxide or contamination layers on the tip and surface are only a few of the effects which may explain a deviation from the theoretical Hertzian contact mechanics.

The experimental in-plane stiffness for fused silica is always lower than 150 N m^{-1}, while for nickel the maximum k_S is lower than 200 N m^{-1}. The stiffness ratio, k_S/k_N, is lower than 0.05 for fused silica and 0.07 for nickel. This result does not agree with the theoretical relation $2/3 \leqslant k_S/k_N \leqslant 18/19$ following from contact mechanics [31]. The high spring constant along

[5] MaTeck GmbH, Germany; fused silica plate SQ1, size 10 mm × 10 mm, thickness 1 mm.

the longitudinal axis of the cantilever (X-axis), a combination of lateral and buckling stiffnesses, produces a high in-plane force. Probably, the in-plane forces are so high that the tip starts to slip on the surface sample. This has to be examined in more detail. For the FEM simulations presented here, a very high elastic modulus was assigned to the elements of the tip in order to avoid the unrealistic deformation of the tip-end due to external forces, i.e. a point load. A more realistic FEM model considering the elasticity of the sensor tip in relation to its special structure and the contact mechanics has to be developed.

Furthermore, to obtain precise quantitative measurements with AFAM, the wear of the tip should be prevented by using wear-resistant layers like diamond and a strict control of the ambient conditions [32] for the tip–sample contact should be maintained.

7. Summary and conclusions

In this work, AFAM measurements on fused silica and nickel single crystals were numerically modeled by FEM to obtain the out-of-plane, k_N, and in-plane, k_S, contact stiffness values. We developed an FEM model, which considers the main geometrical features of commercial stiff cantilevers as well as the elastic anisotropy of silicon single crystals. We fitted this FEM model to a commercially available cantilever in a two-step procedure using the free and contact-resonances of the first and the third bending mode. With the FEM model presented here, we were able to simulate the resonance frequencies of cantilevers more precisely than even with advanced analytical models, which take into account the trapezoidal cross section of the cantilever. The normal spring constant for a cantilever inclined relative to the sample surface was determined by FEM. We used this spring constant value to calculate the static force from the static cantilever deflection. The obtained normal contact stiffness values are within the range covered by the theoretical values for nickel and for fused silica calculated with the Hertzian contact model and a tip radius of 80 nm. The obtained in-plane surface stiffness values k_S are much too low compared with contact mechanics theories, that is, k_S cannot be associated with the reduced shear modulus of the contact. More likely, k_S is related to tip–surface interactions involving water layers and pollution adhered to the tip and the surface. In order to examine the contact forces, especially the lateral forces, in more detail, a more realistic FEM model considering the elasticity of the sensor tip and precise contact mechanics has to be developed. Such a model is challenging, as it will have to cover two different length scales, the μm scale of the cantilever, and the nm scale of the tip–sample contact region.

Acknowledgments

This work was supported by the German Science foundation DFG, by CONACYT in Mexico and by a grant from the Ministry of Science and Technology BMBF fostering international collaboration, via the International Bureau at the DLR Cologne, Germany.

Appendix A. Elastic constants of the cantilever in the Cartesian coordinate systemof the cantilever geometry

In the generalized Hooke's law, the second-order stress tensor σ_{ij} is connected with the second-order strain tensor ε_{kl} by the linear transformation $\sigma_{ij} = C_{ijkl}\varepsilon_{kl}$. The indices

Table A.1. Relation of index pairs in the tensor notation to indices in the matrix notation [33].

Tensor notation	11	22	33	23, 32	13, 31	12, 21
Matrix notation	1	2	3	4	5	6

$i, j, k, l = 1, 2, 3, 4$ describe a Cartesian coordinate system. The elastic constants C_{ijkl} form a tensor of fourth order with 81 coefficients. The symmetry of stress and strain ($\sigma_{ij} = \sigma_{ji}$, $\varepsilon_{kl} = \varepsilon_{lk}$) and the conservation law of energy reduce the number of independent coefficients C_{ijkl} to 21 ($C_{ijkl} = C_{jikl} = C_{ijlk} = C_{lkij}$) allowing a matrix representation of the elasticity tensor. Table A.1 relates the tensor and the matrix notation (e.g. [33]).

Material (e.g. single crystal) symmetry further reduces the number of independent elastic constants. In the case of cubic symmetry, as e.g. for silicon single crystals, three coefficients, C_{11}, C_{12} and C_{44}, remain forming the elasticity matrix $C_{\nu\mu}$ ($\nu, \mu = 1, \ldots, 6$) [33]:

$$C_{\nu\mu} = \begin{bmatrix} C_{11} & C_{12} & C_{12} & & & \\ C_{12} & C_{11} & C_{12} & & & \\ C_{12} & C_{12} & C_{11} & & & \\ & & & C_{44} & & \\ & & & & C_{44} & \\ & & & & & C_{44} \end{bmatrix}. \tag{A.1}$$

For the description of single-crystal silicon AFM cantilevers, a Cartesian coordinate system is chosen with the $1(x)$-, $2(y)$- and $3(z)$-axis in length, thickness and width direction of the cantilever, which coincide with the single crystal directions [110], [001] and [1$\bar{1}$0], respectively. This system is related to the single crystal system {[100], [010], [001]} by two rotations, of 45° around the z-axis and of 90° around the new x-axis.

Two Cartesian coordinate systems of different orientation, (x, y, z) and (x', y', z'), are related by a rotation matrix D, the elements of which a_{ij} are the direction cosines of the new axes, i.e.

$$\begin{bmatrix} x' \\ y' \\ z' \end{bmatrix} = \begin{bmatrix} a_{11} & a_{12} & a_{13} \\ a_{21} & a_{22} & a_{23} \\ a_{31} & a_{32} & a_{33} \end{bmatrix} \begin{bmatrix} x \\ y \\ z \end{bmatrix}. \tag{A.2}$$

For the elastic constants C_{ijkl} forming a fourth-order tensor, the rotation matrix D yields a corresponding transformation matrix which, in matrix notation, is given by [34]

$$R = \begin{bmatrix} a_{11}^2 & a_{12}^2 & a_{13}^2 & 2a_{12}a_{13} & 2a_{13}a_{11} & 2a_{11}a_{12} \\ a_{21}^2 & a_{22}^2 & a_{23}^2 & 2a_{22}a_{23} & 2a_{23}a_{21} & 2a_{21}a_{22} \\ a_{31}^2 & a_{32}^2 & a_{33}^2 & 2a_{32}a_{33} & 2a_{33}a_{31} & 2a_{31}a_{32} \\ a_{21}a_{31} & a_{22}a_{32} & a_{23}a_{33} & a_{22}a_{33}+a_{23}a_{32} & a_{21}a_{33}+a_{23}a_{31} & a_{22}a_{31}+a_{21}a_{32} \\ a_{31}a_{11} & a_{32}a_{12} & a_{33}a_{13} & a_{13}a_{32}+a_{12}a_{33} & a_{13}a_{31}+a_{11}a_{33} & a_{11}a_{32}+a_{12}a_{31} \\ a_{11}a_{21} & a_{12}a_{22} & a_{13}a_{23} & a_{12}a_{23}+a_{13}a_{22} & a_{13}a_{21}+a_{11}a_{23} & a_{11}a_{22}+a_{12}a_{21} \end{bmatrix}, \tag{A.3}$$

$$C'_{\nu\mu} = RC_{\nu\mu}R^{\mathrm{T}}. \tag{A.4}$$

These general equations yield the special results that are appropriate here

$$D_{45^\circ-90^\circ} = \begin{bmatrix} \cos 45^\circ & \cos 315^\circ & \cos 90^\circ \\ \cos 270^\circ & \cos 90^\circ & \cos 0^\circ \\ \cos 315^\circ & \cos 225^\circ & \cos 90^\circ \end{bmatrix} = \begin{bmatrix} \frac{1}{\sqrt{2}} & \frac{1}{\sqrt{2}} & 0 \\ 0 & 0 & 1 \\ \frac{1}{\sqrt{2}} & -\frac{1}{\sqrt{2}} & 0 \end{bmatrix}, \tag{A.5}$$

$$R_{45^\circ-90^\circ} = \begin{bmatrix} \frac{1}{2} & \frac{1}{2} & 0 & 0 & 0 & 1 \\ 0 & 0 & 1 & 0 & 0 & 0 \\ \frac{1}{2} & \frac{1}{2} & 0 & 0 & 0 & -1 \\ 0 & 0 & 0 & -\frac{1}{\sqrt{2}} & \frac{1}{\sqrt{2}} & 0 \\ \frac{1}{2} & -\frac{1}{2} & 0 & 0 & 0 & 0 \\ 0 & 0 & 0 & \frac{1}{\sqrt{2}} & \frac{1}{\sqrt{2}} & 0 \end{bmatrix}, \tag{A.6}$$

$$C'_{\nu\mu} = \begin{bmatrix} \frac{1}{2}(C_{11}+C_{12})+C_{44} & C_{12} & \frac{1}{2}(C_{11}+C_{12})-C_{44} & & & \\ C_{12} & C_{11} & C_{12} & & & \\ \frac{1}{2}(C_{11}+C_{12})-C_{44} & C_{12} & \frac{1}{2}(C_{11}+C_{12})+C_{44} & & & \\ & & & C_{44} & & \\ & & & & \frac{1}{2}(C_{11}-C_{12}) & \\ & & & & & C_{44} \end{bmatrix}. \tag{A.7}$$

Finally, with the elastic constants of single crystal silicon from [27, 28] $C_{11} = 166\,\text{GPa}$, $C_{12} = 64\,\text{GPa}$, $C_{44} = 80\,\text{GPa}$, we obtain

$$C'_{\nu\mu}[\text{GPa}] = \begin{bmatrix} 195 & 64 & 35 & & & & \\ 64 & 166 & 64 & & & & \\ 35 & 64 & 195 & & & & \\ & & & 80 & & & \\ & & & & 51 & & \\ & & & & & 80 & \end{bmatrix}. \tag{A.8}$$

In engineering, instead of the elastic constants $C'_{\nu\mu}$, Young's and shear moduli E′ and G′ and Poisson's ratio ν' are used, which are related to the compliance matrix $C'^{-1}_{\nu\mu}$ by [35]:

$$C'^{-1}_{\nu\mu} = \begin{bmatrix} \frac{1}{E'_x} & -\frac{\nu'_{yx}}{E'_y} & -\frac{\nu'_{zx}}{E'_z} & & & \\ -\frac{\nu'_{xy}}{E'_x} & \frac{1}{E'_y} & -\frac{\nu'_{zy}}{E'_z} & & & \\ -\frac{\nu'_{xz}}{E'_x} & -\frac{\nu'_{yz}}{E'_y} & \frac{1}{E'_z} & & & \\ & & & \frac{1}{G'_{yz}} & & \\ & & & & \frac{1}{G'_{xz}} & \\ & & & & & \frac{1}{G'_{xy}} \end{bmatrix}. \tag{A.9}$$

From equation (A.7) the compliance matrix $C'^{-1}_{\nu\mu}$ follows as

$$C'^{-1}_{\nu\mu} = \begin{bmatrix} \frac{C_{\text{den}} + 2C_{11}C_{44}}{4C_{44}C_{\text{den}}} & -\frac{C_{12}}{C_{\text{den}}} & -\frac{C_{\text{den}} - 2C_{11}C_{44}}{4C_{44}C_{\text{den}}} & & & \\ -\frac{C_{12}}{C_{\text{den}}} & \frac{C_{11} + C_{12}}{C_{\text{den}}} & -\frac{C_{12}}{C_{\text{den}}} & & & \\ -\frac{C_{\text{den}} - 2C_{11}C_{44}}{4C_{44}C_{\text{den}}} & -\frac{C_{12}}{C_{\text{den}}} & \frac{C_{\text{den}} + 2C_{11}C_{44}}{4C_{44}C_{\text{den}}} & & & \\ & & & \frac{1}{C_{44}} & & \\ & & & & \frac{2}{C_{11} - C_{12}} & \\ & & & & & \frac{1}{C_{44}} \end{bmatrix}, \tag{A.10}$$

Table A.2. Elastic constants of the used single-crystal silicon AFM cantilever.

Young's moduli (GPa)	$E'_x = 169.7$	$E'_y = 130.4$	$E'_z = 169.7$
Shear moduli (GPa)	$G'_{xy} = 80$	$G'_{yz} = 80$	$G'_{xz} = 51$
Poisson's ratio	$\nu'_{xz} = \nu'_{zx} = 0.061$	$\nu'_{xy} = \nu'_{zy} = 0.362$	$\nu'_{yx} = \nu'_{yz} = 0.278$

$$C_{\text{den}} = C_{11}^2 + C_{11}C_{12} - 2C_{12}^2. \tag{A.11}$$

The final results used in the numerical simulations are shown in table A.2.

Appendix B. Torsional stiffness of a beam with constant trapezoidal cross section

The torsional stiffness of a beam with constant cross section of trapezoidal symmetry can be derived approximately from the strain energy of the twisted beam [23]. We describe the beam in a Cartesian coordinate system with the x-axis in length direction and the cross section in the y–z-plane (figure B.1).

The shear stresses σ_{yx} and σ_{zx} acting in the cross section of the beam are the spatial derivatives of a so-called stress function $\phi(y, z)$:

$$\frac{\partial\phi(y,z)}{\partial y} = \sigma_{yx}(y,z), \qquad \frac{\partial\phi(y,z)}{\partial z} = \sigma_{zx}(y,z). \tag{B.1}$$

In general, the stress function $\phi(y, z)$ can be represented by an infinite polynomial series in its variables y and z. Additionally, $\phi(y, z)$ has to be zero at the boundaries of the beam, i.e. at $y = h$ or $y = 0$ and $z = \pm(b–(b–a)y/h)$. The boundary conditions are satisfied by the special polynomial

$$\phi_b(y,z) = \left(z - \frac{b-a}{h}y + b\right)\left(z + \frac{b-a}{h}y - b\right)(y-h)\,y, \tag{B.2}$$

and thus, the stress function can be presented in the general form

$$\phi(y,z) = \phi_b(y,z) \sum_{n=1,2,\ldots} \sum_{m=1,2,\ldots} a_{mn} z^m y^n. \tag{B.3}$$

The coefficients a_{mn} (m, n = 0, 1, 2, ...) follow from the strain energy, which for the anisotropic twisted beam is given by

$$U = \int_{-b}^{b}\int_{0}^{h} \left\{\frac{1}{2}\left[\frac{1}{G'_{xy}}\left(\frac{\partial\phi(y,z)}{\partial z}\right)^2 + \frac{1}{G'_{xz}}\left(\frac{\partial\phi(y,z)}{\partial y}\right)^2 - 2\tau\phi(y,z)\right] \mathrm{d}y\,\mathrm{d}z\right\}. \tag{B.4}$$

Here, G'_{ij} are the elastic shear moduli of the cantilever beam in its geometric coordinate system (see appendix A) and τ is the angle of the rotation per unit length. The energy has to fulfil the variational principle $\delta U/\delta\phi = 0$, entailing the conditions $\delta U/\delta a_{mn} = 0$ for each a_{mn}, because polynomials form an orthogonal system. This yields a system of equations determining the coefficients a_{mn}. Because of the symmetry in the z-direction (see figure B.1), only even powers

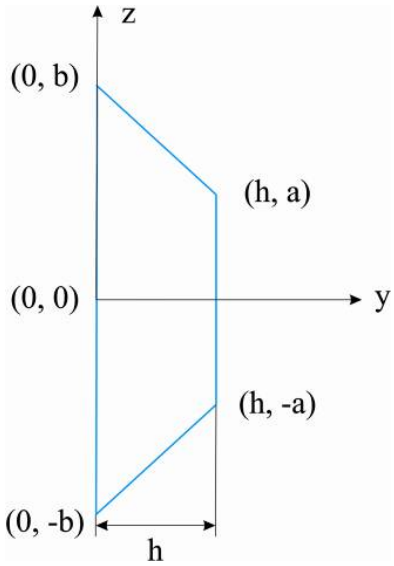

Figure B.1. Schematic of the cross section of a beam with trapezoidal symmetry.

of z may occur, and because of the finite extent of the cross section, only a limited number of terms have to be taken into account depending on the required accuracy. In the case presented here, we found out that the terms up to sixth order in the spatial coordinates, i.e. 15 coefficients, are sufficient within the numerical accuracy we were able to achieve.

Finally, the torque M and the torsional stiffness are given by

$$M = 2\int_{-b}^{b}\int_{0}^{h}\phi(y,z)\mathrm{d}y\,\mathrm{d}z \quad \text{and} \quad C_t = \frac{M}{\tau}, \tag{B.5}$$

respectively.

References

[1] Binnig G, Quate C F and Gerber C 1986 Atomic force microscope *Phys. Rev. Lett.* **56** 930
[2] Brukman M J and Bonnell D A 2008 Probing physical properties at the nanoscale *Phys. Today* **61** 36
[3] Rabe U, Amelio S, Kester E, Scherer V, Hirsekorn S and Arnold W 2000 Quantitative determination of contact stiffness using atomic force acoustic microscopy *Ultrasonics* **38** 430
[4] Yamanaka K, Noguchi A, Tsuji T, Koike T and Goto T 1999 Quantitative material characterization by ultrasonic AFM *Surf. Interface Anal.* **27** 600
[5] Crozier K B, Yaralioglu G G, Degertekin F L, Adams J D, Minne S C and Quate C F 2000 Thin film characterization by atomic force microscopy at ultrasonic frequencies *Appl. Phys. Lett.* **76** 1950
[6] Hurley D C 2009 Contact resonance force microscopy techniques for nanomechanical measurements *Applied Scanning Probe Methods* vol XI ed B Bhushan and H Fuchs (Berlin: Springer) chapter 5, p 97
[7] Rabe U 2006 Atomic force acoustic microscopy *Applied Scanning Probe Methods* vol II ed B Bhushan and H Fuchs (Berlin: Springer) chapter 2, p 37
[8] Rabe U, Hirsekorn S, Reinstädtler M, Sulzbach T, Lehrer Ch and Arnold W 2007 Influence of the cantilever holder on the vibrations of AFM cantilevers *Nanotechnology* **18** 044008
[9] Rabe U, Amelio S, Kopycinska M, Hirsekorn S, Kempf M, Göken M and Arnold W 2002 Imaging and measurement of local mechanical material properties by atomic force acoustic microscopy *Surf. Interface Anal.* **33** 65

[10] Arinero R and Lévêque G 2003 Vibration of the cantilever in force modulation microscopy analysis by a finite element model *Rev. Sci. Instrum.* **74** 104
[11] Song Y and Bhushan B 2006 Simulation of dynamic modes of atomic force microscopy using 3D finite element *Ultramicroscopy* **106** 847
[12] Behrens I, Doering L and Peiner E 2003 Piezoresistive cantilever as portable micro force calibration standard *J. Micromech. Microeng.* **13** S171
[13] Mendels D A, Lowe M, Cuenat A, Cain M G, Vallejo E, Ellis D and Mendels F 2006 Dynamic properties of AFM cantilevers and the calibration of their spring constants *J. Micromech. Microeng.* **16** 1720
[14] Drobek T, Stark R W and Heckl W M 2001 Determination of shear stiffness based on thermal noise analysis in atomic force microscopy: passive overtone microscopy *Phys. Rev.* B **64** 045401
[15] Chen K-N and Huang J-C 2005 Analysis of tip effects on the dynamic characteristics of V-shaped atomic force microscope probes *Proc. 2005 IEEE Int. Conf. on MEMS NANO and Smart Systems (ICMENS '05)*
[16] Hurley D C, Shen K, Jennett N M and Turner J A 2003 Atomic force acoustic microscopy methods to determine thin-film elastic properties *J. Appl. Phys.* **94** 2347
[17] Espinoza-Beltrán F J, Muñoz-Saldaña J, Torres-Torres D, Torres-Martínez R and Schneider G A 2006 AFM cantilever simulation by finite element for quantitative AFAM measurements *J. Mater. Res.* **21** 3072–9
[18] Sulzbach T 2006 NanoWorld Services GmbH private communication
[19] ANSYS Inc. *ANSYS-Engineering Analysis System V10* Version 5.7.1 (Canonsburg, PA: ANSYS Inc.)
[20] Rajakumar C and Rogers C R 1992 The Lanczos algorithm applied to unsymmetric generalized eigenvalue problem *Int. J. Numer. Methods Eng.* **32** 1009
[21] Reinstaedtler M, Rabe U, Scherer V, Turner J A and Arnold W 2003 Imaging of flexural and torsional resonance modes of atomic force microscopy cantilevers using optical interferometry *Surf. Sci.* **532–535** 1152–8
[22] SAS IP Inc. 2007 *ANSYS Release 11. Documentation for ANSYS (Design Optimization)*
[23] Timoschenko S P and Goodier J N 2006 *Theory of Elasticity* (New York: McGraw-Hill)
[24] Johnson K L 1985 *Contact Mechanics* (Cambridge: Cambridge University Press)
[25] Vlassak J J and Nix W D 1993 Indentation modulus of elastically anisotropic half spaces *Phil. Mag.* A **67** 1045
[26] Rabe U, Kopycinska M, Hirsekorn S, Muñoz-Saldaña J, Schneider G A and Arnold W 2002 High resolution characterization of piezoelectric ceramics by ultrasonic scanning force microscopy techniques *J. Phys. D: Appl. Phys.* **35** 2621
[27] Wortman J J and Evans R A 1965 Young's modulus, shear modulus, and Poisson's ratio in silicon and germanium *J. Appl. Phys.* **36** 153
[28] Simmons G and Wang H 1971 *Single Crystal Elastic Constants and Calculated Aggregate Properties: A Handbook* (Cambridge, MA: MIT Press)
[29] Chung K-H, Lee Y-H and Kim D-E 2005 Characteristics of fracture during the approach process and wear mechanism of a silicon AFM tip *Ultramicroscopy* **102** 161
[30] Kopycinska-Müller M, Geiss R H and Hurley D C 2006 Contact mechanics and tip shape in AFM-based nanomechanical measurements *Ultramicroscopy* **106** 466
[31] Mazeran P-E and Loubet J-L 1997 Force modulation with a scanning force microscope: an analysis *Tribol. Lett.* **3** 125
[32] Hurley D C, Kopycinska-Müller M, Julthongpiput D and Fasolka M J 2006 Influence of surface energy and relative humidity on AFM nanomechanical contact stiffness *Appl. Surf. Sci.* **253** 1274
[33] Truell R, Elbaum C and Chick B B 1969 *Ultrasonic Methods in Solid State Physics* (New York: Academic)
[34] Lieberman D S and Zirinsky S 1956 A simplified calculation for the elastic constants of arbitrarily oriented single crystals *Acta Crystallogr.* **9** 431
[35] 2005 Structural Mechanics Module User's Guide (Comsol Multiphysics 3.2) http://www.fermilab.de